

See discussions, stats, and author profiles for this publication at: <https://www.researchgate.net/publication/51666113>

# Initiation and Inhibition of Dealloying of Single Crystalline Cu<sub>3</sub>Au (111) Surfaces

ARTICLE *in* JOURNAL OF THE AMERICAN CHEMICAL SOCIETY · SEPTEMBER 2011

Impact Factor: 12.11 · DOI: 10.1021/ja2054644 · Source: PubMed

CITATIONS

28

READS

88

10 AUTHORS, INCLUDING:



**Asif Bashir**

Max Planck Institute for Iron Research GmbH

50 PUBLICATIONS 544 CITATIONS

[SEE PROFILE](#)



**Genesis Ngwa Ankah**

Leibniz-Institute for New Materials

19 PUBLICATIONS 106 CITATIONS

[SEE PROFILE](#)



**Yvonne Grunder**

University of Liverpool

28 PUBLICATIONS 218 CITATIONS

[SEE PROFILE](#)



**Frank Uwe Renner**

Hasselt University

73 PUBLICATIONS 757 CITATIONS

[SEE PROFILE](#)

# Initiation and Inhibition of Dealloying of Single Crystalline Cu<sub>3</sub>Au (111) Surfaces

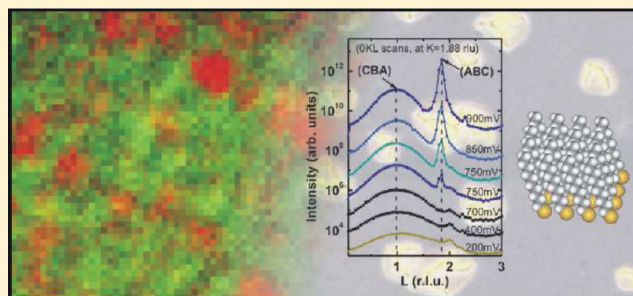
Aparna Pareek,<sup>†</sup> Sergiy Borodin,<sup>†,§</sup> Asif Bashir,<sup>†,§</sup> Genesis Ngwa Ankah,<sup>†,§</sup> Patrick Keil,<sup>†</sup> Gerald A. Eckstein,<sup>†</sup> Michael Rohwerder,<sup>†</sup> Martin Stratmann,<sup>†</sup> Yvonne Gründer,<sup>‡</sup> and Frank Uwe Renner<sup>\*,†</sup>

<sup>†</sup>Max-Planck-Institut für Eisenforschung, Max-Planck-Straße 1, D-40237 Düsseldorf, Germany

<sup>‡</sup>European Synchrotron Radiation Facility, BP220, F-38043 Grenoble, France

 Supporting Information

**ABSTRACT:** Dealloying is widely utilized but is a dangerous corrosion process as well. Here we report an atomistic picture of the initial stages of electrochemical dealloying of the model system Cu<sub>3</sub>Au (111). We illuminate the structural and chemical changes during the early stages of dissolution up to the critical potential, using a unique combination of advanced surface-analytical tools. Scanning tunneling microscopy images indicate an interlayer exchange of topmost surface atoms during initial dealloying, while scanning Auger-electron microscopy data clearly reveal that the surface is fully covered by a continuous Au-rich layer at an early stage. Initiating below this first layer a transformation from stacking-reversed toward substrate-oriented Au surface structures is observed close to the critical potential. We further use the observed structural transitions as a reference process to evaluate the mechanistic changes induced by a thiol-based model-inhibition layer applied to suppress surface diffusion. The initial ultrathin Au layer is stabilized with the intermediate island morphology completely suppressed, along an anodic shift of the breakdown potential. Thiol-modification induces a peculiar surface microstructure in the form of microcracks exhibiting a nanoporous core. On the basis of the presented atomic-scale observations, an interlayer exchange mechanism next to pure surface diffusion becomes obvious which may be controlling the layer thickness and its later change in orientation.



## 1. INTRODUCTION

Many electrochemical processes still lack fundamental understanding, which is often due to the complexity of the involved systems and the special challenges for in situ characterization. One prime example, dealloying, also termed as selective dissolution or leaching, is a specific corrosion process contributing to perilous materials deterioration.<sup>1–5</sup> About 25% of the huge cost to society because of corrosion could be saved by better corrosion knowledge and management.<sup>1</sup> However, this process is also of pivotal technological importance. Historically, dealloying was already used in ancient societies,<sup>6</sup> and in 1928, Raney invented the well-known dealloyed catalyst Raney nickel.<sup>7</sup> A similar methodology is used today for the most active catalyst particles for the oxygen reduction in fuel cells<sup>8–10</sup> which are prepared by dealloying of a Cu–Pt nanoparticle precursor. Several further applications from catalytic materials to sensors<sup>11–20</sup> were recently proposed for nanoporous metals which are obtained by dealloying of bulk alloys. Despite the thus fundamental importance of dealloying, key features are, with first successful steps, not yet predictable and often unknown. Important issues are the structure, stability, and composition of the forming passive-like surface films or the processes leading to their breakdown at the so-called critical potential ( $E_c$ ). While several important approaches have been discussed,<sup>21–25</sup>

only few atomistic simulations have been performed.<sup>26</sup> Also the critical pit diameter as well as related surface and interface energies were considered in a purely thermodynamic approach.<sup>24,25</sup> However, also the role of kinetic effects and surface diffusion was often emphasized in dealloying.<sup>27–32</sup> Microscopic atomic-scale observations, also needed to evaluate any simulation result, are still rare but will benefit the understanding of stability of structural materials as well as of catalyst alloy nanoparticles.

The simplest scenario of dealloying occurs, if a binary alloy of elements with sufficiently different equilibrium potentials is exposed to an acidic electrolyte in which no stable bulk oxide is formed. Cu and Au are elements of largely different equilibrium potential values ( $E_e$ ). Also they possess a large difference in respective lattice parameters (13%) which makes the initial processes of dealloying in this system naturally addressable by X-ray diffraction. Above  $E_c$ , the entire crystal transforms into a nanoporous network of the nobler element.<sup>33</sup> Below  $E_c$ , the more reactive element (here Cu) of a freshly exposed Cu<sub>3</sub>Au alloy initially dissolves, but a passive noble metal film is formed.<sup>34</sup> With the initial dissolution of Cu above  $E_c$ , an epitaxial ultrathin

Received: June 21, 2011

Published: September 27, 2011

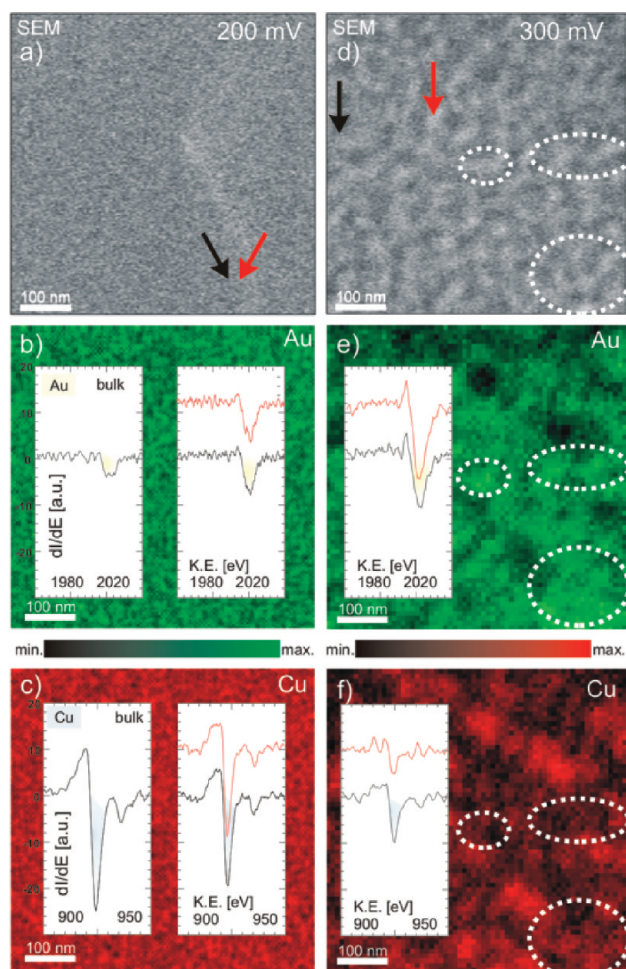


**Figure 1.** Ex-situ elemental analysis by scanning Auger-electron microscopy of selectively dissolved  $\text{Cu}_3\text{Au}$  (111) surfaces in 0.1 M  $\text{H}_2\text{SO}_4$ . Color code is from minimum to maximum signal at each map and potential. The specimens were polarized 1 h at lower potentials (a–c) 200 mV and (d–f) 300 mV. The SEM images and respective elemental maps of the same area of Au and Cu along with corresponding spectra (insets) are shown. The colored arrows in the SEM images indicate the positions for the respective inset Auger spectra. Potentials are referenced to a Ag/AgCl electrode.

Au-rich layer forms<sup>35–38</sup> possessing an inverted CBACB stacking sequence compared to the  $\text{L}_{12}$   $\text{Cu}_3\text{Au}$  (111) substrate (ABC...). The ultimately important potential region closer to and at  $E_c$  has to our knowledge not been probed in detail before. Knowledge of the developing chemical surface compositions as well as structural surface investigations were still missing. Here we present a comprehensive experimental study observing selective dissolution from a bare  $\text{Cu}_3\text{Au}$  (111) surface in pure 0.1 M sulfuric acid, as well as with a hexadecanethiol-modified<sup>28</sup> starting surface in the entire passive-like region up to  $E_c$ . The applied thiol self-assembled monolayer (SAM) suppresses Au surface diffusion and allows thus to directly visualize corrosion inhibition and its atomic-scale effects, opening at the same time a route to achieve peculiar surface morphologies.

## 2. EXPERIMENTAL SECTION

The  $\text{Cu}_3\text{Au}$  (111) single crystals were obtained from MaTeck, Germany, and SPL, the Netherlands. The surfaces were prepared by

sputtering and annealing cycles in UHV.  $\text{Cu}_3\text{Au}$  possesses an ordered structure (fcc-like  $\text{L}_{12}$ ) at room temperature. We note that our experiments are not sensitive to the influence of the ordering state of the  $\text{Cu}_3\text{Au}$  substrate as we did not attempt to obtain a well-ordered superstructure with large domains which would require a very accurate control of annealing temperature over many hours.<sup>35</sup> To recover a moderately corroded surface, typically a few sputter/annealing cycles were applied. More deeply dealloyed surfaces had to be repolished. The hexadecanethiol-modified surface was obtained by immersing a well-prepared  $\text{Cu}_3\text{Au}$  (111) crystal in a hexadecane-thiol containing ethanol solution for several hours. The in situ X-ray measurements were performed at the 6-circle diffractometer of the beamline ID32 at the European Synchrotron Radiation Facility (ESRF), using an X-ray energy of 18.2 keV ( $\lambda = 147$  pm). The beam was focused to a vertical spot size at the sample of  $40\text{ }\mu\text{m}$  by a set of compound refractive lenses (CRL) at a focal distance of 15 m from the sample. An incident angle of  $0.3^\circ$  toward the surface plane was chosen. For indexing the reciprocal space we used a coordinate system HKL that was adapted to a hexagonal surface primitive cell such that the reciprocal L-coordinate was oriented along the surface normal.<sup>37</sup> The reciprocal positions are indicated in relative reciprocal units (rlu) with respect to  $\text{Cu}_3\text{Au}$  substrate coordinates. For experiments, the samples were mounted on a thin-film in situ X-ray diffraction cell that was described previously.<sup>39</sup> For the ex-situ AFM images a Dimension 3100 from Molecular Imaging Corporation (Tempe, AZ, USA) was used. The in situ electrochemical STM-study was carried out with a commercial instrument, PicoSPM from Molecular Imaging with a Nanoscope electronic controller. All images were taken in constant current mode with  $I_T = 1$  nA. The STM tips used for the experiments were made of Pt/Ir wire, etched in a 3.5 M NaCN solution and isolated by an electrochemical coating (ZQ 84-3225, BASF, Munster, Germany).<sup>40</sup> A Pt wire was used as a counter electrode and a microreference electrode was used as reference electrode. Auger electron maps were recorded by using a JAMP-9500F scanning Auger microprobe (JEOL, Japan) with an electrostatic hemispherical analyzer. Depending on the signal-to-noise ratio an electron beam of 25 kV and 10 nA or 15 nA at an angle of incidence of  $30^\circ$  was applied. These acquisition conditions lead to high spatial resolution with probe diameters of about 10 nm. More experimental details are available as Supporting Information.

## 3. RESULTS

### 3.1. Detailed Surface Analysis at Lower Overpotentials.

After contact with electrolyte initial selective Cu dissolution takes place and proceeds until a Au-rich passive-like film covers the surface. Surface-sensitive X-ray diffraction (SXRD) results<sup>37</sup> showed the formation of a Au-rich layer at these lower overpotentials, but so far no direct information of the chemical composition and especially the homogeneity and local surface evolution along the surface was available.

The chemical composition variations along the surface have now been probed by ex-situ scanning Auger electron microscopy (SAEM) with a lateral resolution of about 10 nm (Figure 1). The scanning electron microscopy (SEM) image in Figure 1a represents the exact area in which the Au Auger line (Figure 1b) and Cu Auger line (Figure 1c) was recorded. The insets show the respective additional high-resolution parts of the Auger signal. The signals at different positions on the surface show a laterally homogeneous Au enrichment at that early stage (200 mV, 1 h). The map reflects the statistical fluctuations of the measurement and a quantitative line analysis of separately recorded high-resolution spectra (cp. Supporting Information Figure S1) is consistent with one atomic layer of pure Au. At more elevated



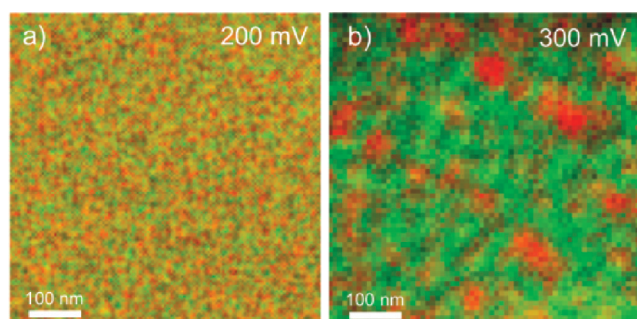


**Figure 2.** Overlay of the respective Cu and Au scanning Auger maps of Figure 1 after 1 h at 200 mV (a) and 300 mV (b).

potentials (300 mV) the situation changed considerably as indicated from Figures 1d–f. The known island formation visible in the SEM image corresponds very well to the Au and Cu Auger signals revealing a nearly pure Au signal from the formed islands and to the signal from also largely Au-enriched valleys between the islands. The visible islands correspond well to nearly pure 25 nm wide and 3 nm thick Au islands, and the deeper parts are in line with a relatively thin (1 nm) film. Figure 2 shows an overlay of the respective Cu and Au Auger maps. The color range of the images is from the minimum to the maximum signal values on the respective samples with the maximum Cu signal being much lower at 300 mV (Compare the inset spectra shown in Figure 1). The Cu signal clearly vanishes with increasing time and potential, but with a different rate at different locations. While in electrolyte the surface-atom mobility of Au<sup>41</sup> is high, we can safely assume the surface structures to be sufficiently static on the time-scale of the Auger microprobe measurements in vacuum. Together with our earlier X-ray results (showing no intermediate intensity between the respective reflections) it therefore becomes immediately clear that a metallic passive-like Au-rich film is finally covering the entire surface. This observation reminds of earlier simulation results for a case below  $E_c$  for the Ag–Au system.<sup>27</sup>

In situ STM measurements were performed in the same lower-potential regime to address the changes in local morphology of the Cu<sub>3</sub>Au (111) surface during Cu dissolution. Figure 3 shows a selection of the obtained potential-dependent STM images of the alloy surface. Supporting Information Figure S2 shows an extended sequence. With UHV preparation, the alloy surface consists of flat monatomic terraces. After immersion of the sample in electrolyte, the terraces and step edges show initiation of the selective dissolution (due to dissolution of surface oxides formed during the short transfer in air), leading to small pits of monolayer depth on the surface. With the increase in potential, the terraces become smoother again, reflecting the high Au surface diffusion in electrolyte (Figure 3a and b). The relative compactness of areas of the second atomic layer was clearly visible after partial dissolution of the topmost surface layer above. The associated relative stability (enrichment in Au atoms) of the lower terrace points directly to an exchange of Cu and Au atoms within the top and second layer during dissolution of the top layer (interlayer exchange). At slightly elevated potentials (Figure 3c and d) the surface showed substantial roughening with an evident increase in depth of the nanometer-scale pits, that is, the dissolution process reached deeper into the material. The increasing roughness hindered further in situ STM imaging. This is also the potential regime where the formation of Au islands was observed<sup>37</sup> by surface-sensitive X-ray diffraction.

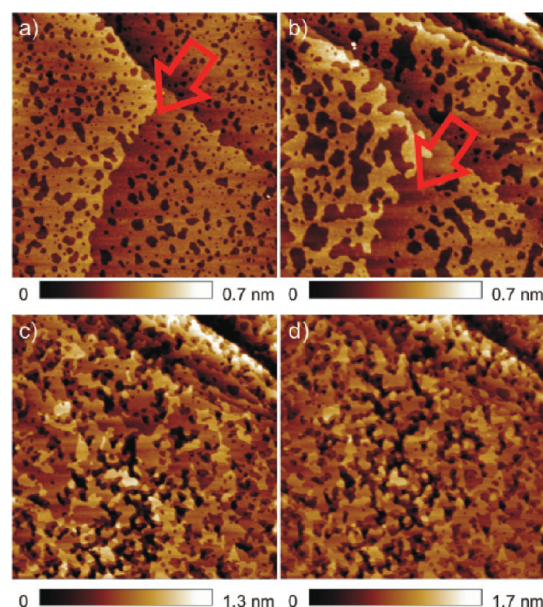


**Figure 3.** Selection of in situ STM images (500 nm × 500 nm) of selective dissolution of a Cu<sub>3</sub>Au (111) surface in 0.1 M H<sub>2</sub>SO<sub>4</sub>. (a) +270 mV,  $t = 174$  min, (b) 330 mV,  $t = 183$  min, (c) 470 mV  $t = 211$  min, (d) 510 mV,  $t = 263$  min. All potentials are referenced to a Ag/AgCl electrode.

These islands inherited the reversed stacking behavior of the ultrathin film. Noteworthy is that the deduced rms roughness of the island-covered surfaces of 1.7 nm is below the observed film thickness (2–3 nm). The detailed Auger microprobe data complement the morphological information from the in situ STM and the earlier (laterally averaging) X-ray data in an unprecedented way: Even on the nanoscopic scale a laterally continuous nearly pure Au layer is formed on the surface already at low overpotentials.

**3.2. Medium Overpotentials and Critical Potential.** Pronounced dealloying irreversibly alters and destroys the elaborately prepared single crystalline surface. Also eventually increasing surface roughness interferes with many high-resolution (in situ) methods e.g. with scanning probe techniques. Therefore higher overpotentials close to or above  $E_c$  had not been applied before, although especially the structural changes around the critical potential are most interesting. X-ray diffraction offers here clear advantages and addresses the topmost surface as well as buried structures below eventual surface layers. Additionally for Cu<sub>3</sub>Au (111), the stacking-reversed initial layers offer to track the surface structures and their growth behavior in a very unique way. The respective Bragg peaks are well separated from substrate intensity and are therefore clearly to detect.

In Figure 4a reciprocal space KL maps around the (0, 2, 1) and (0, 2, 2) substrate positions at different potentials are shown. The reciprocal space is sketched in Figure 4b for comparison. A low-intensity streak decreasing with higher L-values in the left map (–100 mV) at  $K = 1.92$  rlu is already visible after immersion into electrolyte at –100 mV. Such monotonically decreasing X-ray intensity (showing no oscillation of Bragg peak) perpendicular to the respective surface is the direct signature of a single-monolayer (ML) film. Together with relative high background intensity originating from an incomplete, rough surface this directly points to the presence of some patches of 1 ML-thick Au-rich islands and corresponds very well to the described STM images. With a

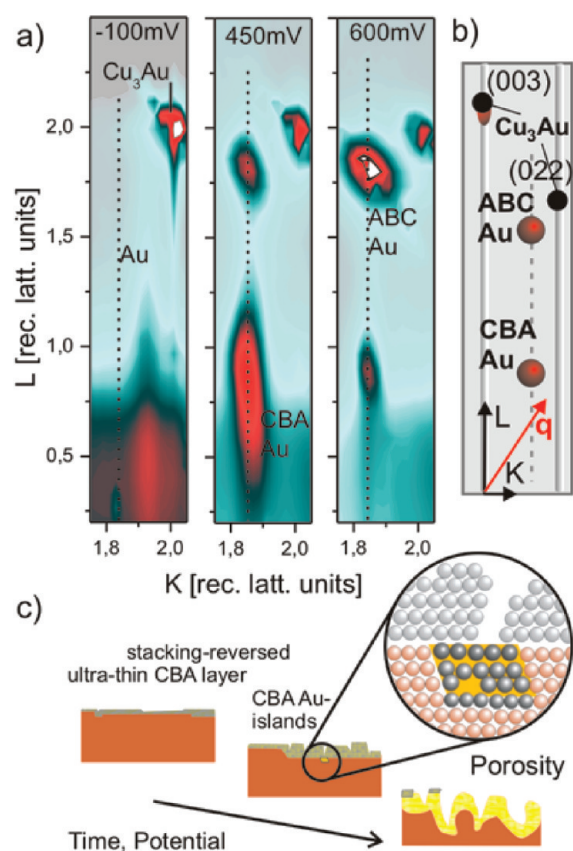


**Figure 4.** In situ X-ray diffraction results. (a) Out-of-plane reciprocal space maps showing the initial crystalline structure of  $\text{Cu}_3\text{Au}$  (111) at  $-100$  mV, the formation of thicker Au islands at  $450$  mV (CBA-Au peak) and substrate-oriented peak at  $600$  mV (ABC Au). The growth of the substrate-oriented ligaments above  $450$  mV (ABC-Au peak) proceeds at the expense of the initial CBA-Au islands. (b) Sketch of reciprocal space of Au/ $\text{Cu}_3\text{Au}$  (111). (c) Sketch of the growth of surface structures as a function of time and potential.

reciprocal position at  $K = 1.92$  the Au-rich monolayer assumes an in-plane lattice parameter nearly identical to the values observed for the slightly thicker 2–3 ML CBA films<sup>37</sup> with  $K$  being about 1.90 rlu. For comparison, the (2, 2, 0) planes of pure Au have a distance of 144 pm, which corresponds to  $K = 1.84$  rlu. The deviation for the ultrathin layers have been attributed partially to a residual Cu content of up to 30% as well as to strain caused by the lattice mismatch at the interface with the substrate and to surface stress. At  $450$  mV the surface is mainly covered with thin stacking-inverted Au-rich islands (CBA-stacking) resulting in the strong broad peak at  $L = 0.8$  rlu. In the final map of Figure 4a at  $600$  mV the dominant peak is at  $L = 1.84$ , corresponding to nearly pure epitaxial, ABC-stacked Au structures. The relative sharp peak is close to the substrate peak at  $L = 2$  (substrate orientation). We thus monitored a change in respective crystallite orientation from CBA to ABC. The corresponding Bragg-peaks are well separated and no interdiffusion zone<sup>21</sup> is found. Intermediate intensity between Bragg peaks would be typical for further intermediate Cu–Au compositions. Figure 4c represents a sketch of the evolving surface morphology. The respective ABC Bragg peaks are sharper in  $L$ -direction than the CBA island peaks and are finally approaching the width of the corresponding in-plane scans and becoming isotropic in shape. The corresponding

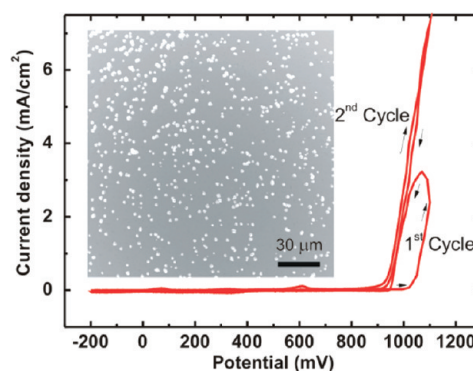


**Figure 5.** Cyclic voltammograms obtained for hexadecanethiol-modified  $\text{Cu}_3\text{Au}$  (111) single crystals in  $0.1$  M  $\text{H}_2\text{SO}_4$ . The scan rate was  $10 \text{ mVs}^{-1}$ . All potentials are referenced to a Ag/AgCl electrode. The inset shows an SEM image of the  $\text{Cu}_3\text{Au}$  (111) single crystal surface after recording the cyclic voltammograms. More details on thiol-modified surfaces are given in Figure 6.

ABC islands (or “substrate-oriented ligaments”) are thus thicker than the initial, inverted Au CBA islands. Such an isotropic peak width is in line with the formation of ligaments of a porous Au structure as it is observed above the critical potential.<sup>33,42</sup> This final growth stage proceeds close to the critical potential. A direct potential step to a higher potential of  $550$  mV, applied to a freshly prepared surface, results in the same structures than in the case of a gradual, stepwise increase (Supporting Information Figures S3 and S4). Our experiments therefore reveal that also for direct potential steps the same sequence in structures occurs and that the formation is mostly dependent on the applied potential and less on time. The respective structures form successively, that is, with increasing thickness of the surface layers. Voltammograms are reported to overestimate the value of  $E_c$  by about  $150 \text{ mV}$ <sup>43</sup>, and we can expect the true  $E_c$  to be around  $650$ – $700$  mV.

The described change in crystallite orientation at higher potentials can be associated with an increasing importance of an interlayer exchange process (as it was observed in the in situ STM at lower potentials above) in addition to the dominating surface diffusion. An interlayer exchange process can preserve the orientation of the substrate for the new Au phases. The substrate-oriented ABC Au structures only emerge after a complete layer of stacking-reversed CBA Au islands has formed on top of the substrate surface. The initial CBA layer quickly vanishes at higher potentials close to  $E_c$ .

**3.3. Dealloying Behavior of Thiol-Modified Surfaces.** Thiol self-assembled monolayers (SAMs) can be considered as well-defined model corrosion-inhibition systems and allow here for directly probing the effect of (suppressed) surface diffusion<sup>28,41</sup> on the forming surface structures.

In the first cycle of the voltammogram for a hexadecanethiol-modified surface (Figure 5) the “critical” potential with a value of about  $1$  V is shifted anodic by about  $100$  mV compared to the behavior in pure sulfuric acid<sup>24,28,44</sup> where the critical potential was at about  $800$ – $900$  mV. In the second cycle, the critical potential in pure sulfuric acid is reproduced and the current rises steeply after reaching  $900$  mV. The inset of Figure 5 shows an SEM image of the surface after the potential cycles. The surface is covered by defects or microcracks with a nanoporous interior, instead of usually obtained homogeneous porosity. Nanoporous Au occupies a smaller volume than the initial alloy<sup>33</sup> and cracking accordingly reveals the formation of large strain created close to



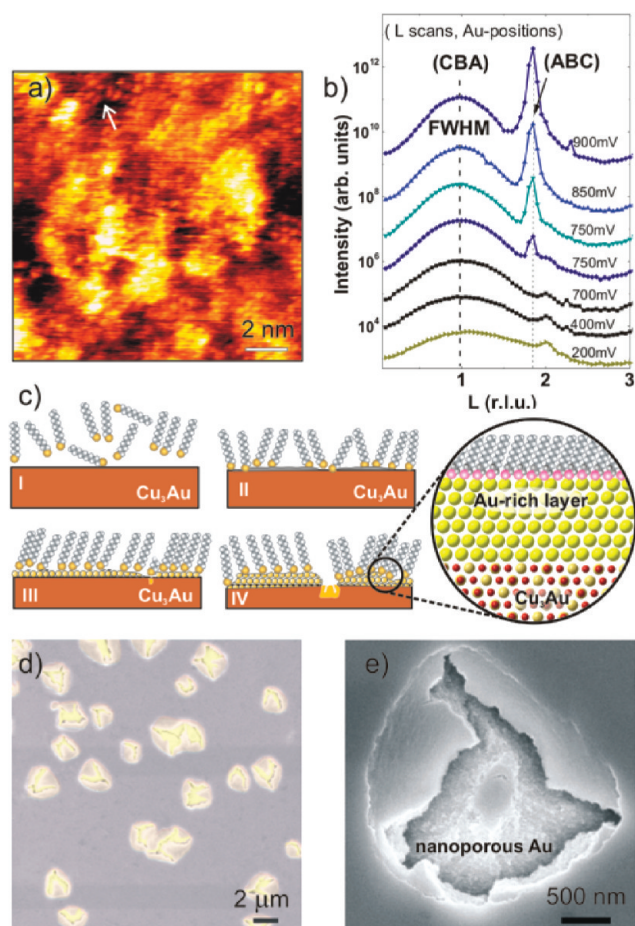


**Figure 6.** (a) Ex-situ STM of a thiol-modified  $\text{Cu}_3\text{Au}$  (111) surface. A short-range ordering is visible. (b) Out-of-plane L-scans recorded as a function of applied potentials on the hexadecanethiol modified  $\text{Cu}_3\text{Au}$  (111) surface in 0.1 M  $\text{H}_2\text{SO}_4$ . The broad peak corresponds to inversely stacked (CBA) ultrathin Au rich layer. At 750 mV the peak corresponding to substrate oriented Au crystallites (ABC Au) appears and grows. (c) Schematic representation of the inhibition effect of thiols. (d) SEM images (cracks slightly colored for clarity, see also Supporting Information Figure S5) of the surfaces after recording the cyclic voltammograms. (e) Enlargement of a microcrack.

the actual dissolution sites. Clearly, the SAMs tremendously stabilize the surface as no island formation, nanometer-scale pit formation or porosity is observed on the thiol-covered, defect-free surface even after applying these high potentials. The dissolution is concentrated to a few crack sites, which are formed every few micrometers. The respective current–potential cycles for the thiol-modified surfaces and the apparent “critical” potential reflect thus an entirely new mechanism and also a unique surface morphology compared to the usual creation of homogeneous nanoporosity in this system. Atomic scale information on a thiol-modified  $\text{Cu}_3\text{Au}$  (111) starting surface could be obtained by ex-situ STM, and during dealloying for the entire passive potential range by in situ SXRD. The ex situ STM image in Figure 6a shows a thiol-induced superstructure, that is, a self-assembled monolayer basically in a  $\sqrt{3} \times \sqrt{3}$  structure, but very small domains and poor order. The alloy surface show monatomic islands but is densely covered with thiol molecules. Structural information is revealed by the out-of-plane in situ SXRD scans in Figure 6b. The first scan after immersion at low

potential indicates already an initial ultrathin Au-rich film which is likely induced by Au segregation due to a preference of the thiol–Au (sulfur–Au) bond over the Cu–S bond during the thiol SAM chemisorption. The ultrathin layer in real space is evidenced by the broad peak ( $\Delta L \approx 1$ ) in reciprocal space. With a first increase of the applied potential, further growth of the signal from the CBA layer could be observed together with a gentle narrowing of the peak width. The low intensity close to  $L = 2$  rlu stems from the background of the large  $\text{Cu}_3\text{Au}$  substrate peak at (0, 2, 2). The first signal from substrate-oriented ABC Au ligaments is emerging only at a well-elevated potential of 750 mV. The peak width is immediately much sharper for the Au ligaments. The transformation potential on a hexadecanethiol-modified surface is about 300 mV higher than that of the corresponding bare  $\text{Cu}_3\text{Au}$  (111) surface. Furthermore, the initial nearly pure Au layer is still stable at this high potential and consists of several atomic monolayers. Thicker Au islands are not formed. The analysis of the diffraction peaks reveals a thickness of 5–7 ML of a nearly pure Au layer, in contrast to the thiol-free surfaces with 3 ML (ultrathin Au-rich layer) or the subsequent Au islands of about 12–15 ML thickness. In addition, the intensity from the inverted initial CBA Au film (inverted stacking) is not decreasing with the formation of porosity at potentials as high as 900 mV. The surface film structure is stabilized in a way that the initial CBA film is present even above the apparent  $E_c$ . Thiols are known to suppress the surface diffusion<sup>28,45</sup> and a ripening process is thus strongly decreased. Figure 6c sketches this mechanistic sequence for the thiol-modified surface. Figure 6d and e show the cracks and their nanoporous core after dealloying. The nature of the initial defects at the sites of crack formation is here not completely clear, but their average distance is far larger than the typical domain size of the SAMs (Figure 6a) and thus not associated to typical structural defects such as domain boundaries of the SAMs. Compared with the otherwise homogeneous formation of nanoporosity, the dealloying mechanism is clearly altered for the thiol-modified surfaces. As a consequence such thiol inhibition layers might be applied to structure surfaces and create nanoporous regions only at desired locations.

#### 4. DISCUSSION

A detailed knowledge of the surface structure and composition is key to the understanding of the operational parameters of dealloying. Residual reactive elements as well as surface strain will alter the reactivity and functionality.<sup>9,17,46</sup> With its peculiar sequence of initial structures,  $\text{Cu}_3\text{Au}$  (111) represents a unique model case for addressing the mechanisms of dealloying in an unprecedented way. During the first steps of dealloying the surface evolves by stripping of the more reactive atoms (here Cu) from the topmost layer.<sup>26,47</sup> Subsequently, an initial ultrathin Au-rich film develops and covers the surface. The Au surface atoms of the formed ultrathin Au-rich surface layer are highly mobile in electrolyte,<sup>41</sup> and the resulting fluctuations in thickness gradually expose also deeper Cu atoms. At slightly elevated potentials the formation of thicker Au islands occurs which inherit the stacking-reversal behavior of the initial layer. As long as the applied potential is below the critical potential, the system shows a passive-like behavior, i.e. the dissolution current falls to very small values. Recent work<sup>24–27,35–38</sup> on dealloying clearly favors surface diffusion as the main reaction path for the formation of the passive-like layer (and beyond). The clear

change in surface morphology by the application of the thiol SAM directly corroborates this assumption.<sup>37,38</sup>

Here, the peak width analysis of our diffraction data provides a thickness of 3–4 ML of the initial ultrathin layer in the case of the clean Cu<sub>3</sub>Au (111). The subsequent Au islands are about 3 nm, or 12–15 ML, thick and about 10–12 nm wide, which is in reasonable agreement with the SEM and STM results. We observed the first nanometer-scale pitting in our in situ STM images in the same range of potential than the island formation registered by in situ SXRD; both observations represent the same process. This structural transition from a rather flat ultrathin Au-rich layer to slightly thicker nearly pure Au islands occurs completely within the passive-like regime well below  $E_c$ . The associated change in surface morphology was confirmed by several techniques (In situ STM, SXRD, AFM, and SEM) and is thus well established on Cu<sub>3</sub>Au (111). Thermodynamically stable nanometer-scale pits are possible at higher overpotentials, which are necessary for allowing for the related extra surface energy. This fact has been discussed<sup>24,25</sup> related to the critical potential itself. On the other side, the transition from the initial ultrathin film to the thicker islands is also a transition from a Au-rich film (max 30% Cu) to nearly pure Au, and from an eventually strained film to relaxed islands. The resulting strain-free pure Au islands show a remarkable homogeneous size distribution and close-packed (hexagonally ordered) arrangement.<sup>37</sup> Therefore, the island formation process can also be seen as a spinodal-like dewetting (without thermodynamic barrier) relaxation step of the growing layer within the clean Cu–Au system. In contrast to the processes on the clean surfaces, application of the thiol SAM layer suppresses the formation of Au islands and the initial Au layer grows to 5–7 ML, i.e. almost double in thickness compared to the clean surface. Furthermore,  $E_c$  shifted positive and massive dealloying above the apparent  $E_c$  occurred only at a limited number of larger cracks, producing a very different surface morphology. Because of similarities to pitting processes occurring on passive oxide-covered metals the “critical” potential might here be called a “pitting” potential. First, we remark that in case we hypothetically could switch off the crack formation  $E_c$  should be even higher. Second, the suppression of dealloying by thiol layers offers the possibility to produce microscale patterns of nanoporous structures. Microstructured thiol layers can be for example applied by microcontact printing<sup>48</sup> ( $\mu$ -CP).

The observed structural transformations, first to Au islands and later to substrate-oriented ABC ligaments, raise additional questions. Mobile Au ad-atoms on the existing initial CBA islands, or after reaching them, will nucleate and continue to grow following the existing inverted, CBA lattice. This is what we observed for the first transition of the ultrathin layer toward the Au islands. Below the critical potential the dissolution rate finally slows down because Cu atoms are hardly exposed directly to the electrolyte after the relatively thick Au islands completely cover the surface. Our SAEM images (Figure.1) reveal a completely Au-covered surface at elevated potentials, with the island morphology clearly developed. Also, Monte Carlo simulations predicted a continuous Au layer on Ag–Au.<sup>27</sup> In addition, we found in our STM study dissolution from terrace sites and the formation of deeper nanometer-scale pits well below  $E_c$ . The evidenced complete coverage of the surface by several atomic monolayers of the nobler species thus rules out earlier explanations of the critical potential being due to direct dissolution from intact original terrace sites.<sup>47</sup> Unexpectedly, at higher applied potentials and after the surface is fully covered by the initial islands,

substrate-oriented structures emerge, which are unambiguously evidenced in our X-ray diffraction data presented in Figure.4. One of the unique strengths of in situ SXRD is to detect structural crystallographic changes within the surface and the buried subsurface region. This is here especially important for monitoring the surface evolution at higher potentials. The change of the stacking-sequence at this point of higher applied potentials appears difficult to understand by surface diffusion alone as the surface is fully covered by islands of the other orientation as mentioned above. Overcoming a few atomic layers by an interlayer-exchange process, might well be possible at room temperature considering the expected high defect density created by the dissolution process. Our STM images evidence interlayer exchange between the topmost atomic layers; and also in electro-deposition of dissimilar metals it is well-known that interface alloying occurs at room temperature. In addition, adsorbate induced surface segregation is a known phenomenon affecting more than the topmost layer also at room temperature, for example, on electrocatalysts.<sup>49</sup> Such an interlayer-exchange process may explain the observation of the stable, several atomic layers thick passive noble metal film with the applied thiol inhibition-layer. Its maximum thickness of 5–7 ML would be a direct measure for its depth of influence. Clearly, this is very different from an extended “bulk” diffusion process as discussed, for example, by Pickering and Wagner.<sup>21</sup> Created vacancies at the solid-electrolyte interface would be transmitted toward the heterophase film—substrate interface in a (limited) vertical diffusion process. The substrate vacancies will eventually be filled by neighboring Au atoms to form Au crystallites which will naturally inherit the crystal structure (stacking sequence) from the initial substrate. Once the creation and further growth of substrate-oriented Au clusters or ligaments started to proceed into the bulk, the initial CBA islands will vanish in a ripening process because of the still high surface diffusion. The observed interlayer exchange mechanism should be active also in other noble metal alloys, like Cu–Pd or Co–Pt.

The presented detailed experimental insight into the atomic processes at the different stages of dealloying offer to gain further understanding by advanced simulations. Our own efforts target currently the stability of the CBA ultrathin Au film on Cu<sub>3</sub>Au (111) as well as the structure of the heterophase interface (Supporting Information Figure S6).<sup>50</sup> The role of vacancies in diffusion processes is recognized since Kirkendall<sup>51</sup> but bulk diffusion is too slow at room temperature to play a significant role. Explanations using enhanced double-vacancy diffusion<sup>21</sup> were not widely accepted.<sup>52</sup> Nevertheless, because of significant structural changes close to the surface, interlayer-exchange processes are likely to be facilitated close to ultrathin layers and the often incoherent heterophase interfaces. Beyond the creation of surface vacancies by the Cu dissolution also structural defects such as misfit dislocations at the buried heterophase film—substrate interface are involved and should influence the vertical transport across the surface region. A clearer picture should emerge from more detailed simulations of this elaborate surface film structure, but the problems to tackle are challenging. First, a precise description<sup>54</sup> of solid–liquid and solid–electrolyte interfaces is just at the beginning, but important for addressing the surface diffusion, solubility, or dissolution rates. Second, the unit cell to describe heterophase interfaces for ab initio calculations is large. With the 5% lattice mismatch of the Au-rich film and the substrate (peaks at  $H = K = 1.9$  rlu and 2 rlu, respectively) a super cell describing the structural configuration needs to include  $20 \times 20$  atoms per atomic layer, amounting to at least 2000 Cu and Au



atoms. Large-scale molecular dynamics simulations, on the other hand, often depend critically on the chosen atomic potentials. Despite the challenge, modern computing systems should become increasingly powerful in the near future to address even more complicated structures. Our study directly shows that interlayer exchange processes are active on the topmost surface. This additional aspect will be important to consider in modeling and simulation, especially in systems developing lattice strain during dealloying. The growth of the initial layer especially calls for refined simulations as both, interlayer exchange and surface diffusion contribute. Detailed values of the respective diffusion coefficients, e.g. along interfaces, are still widely unknown. An important part of our work has been to directly address the surface diffusion by the application of a surface SAM. Thiol films were predicted to stabilize surface vacancies on Au substrates<sup>53</sup> and local strain and interface dislocations<sup>50</sup> might increase the diffusion across the layer in the Cu–Au system. Our detailed findings on structure and composition during the initial stages of dealloying offer a benchmark scenario for future advanced materials simulations.

## 5. CONCLUSION

We have presented a detailed atomic-scale picture of the initial steps of potential-induced selective dissolution of Cu from clean and hexadecanethiol-modified Cu<sub>3</sub>Au (111) in 0.1 M H<sub>2</sub>SO<sub>4</sub>. Our X-ray experiments were fully spanning potentials within the entire regime of passivation up to E<sub>c</sub>. We observed the known first stacking-inverted (CBA) metallic passivation layer to cover the entire surface and to transform close to E<sub>c</sub> into solely substrate-oriented (ABC) Au crystallites. This finding points to an interlayer exchange process in parallel to surface diffusion, what is supported by an STM study. We have studied the effect of a hexadecanethiol-modified surface which stabilized the initial ultrathin Au layer (opening a route to structured nanoporous surfaces e.g. for membranes). Studies on the mechanisms of corrosion inhibition, especially with atomic-scale detail, are rare. With our hexadecanethiol-modified surface we applied a model inhibitor film to suppress surface diffusion during the first steps of dealloying. The formation of islands in the passive region was completely suppressed with the applied thiol-film, and substrate-oriented Au ligaments were observed only within crack-pits at very high potentials, about 350 mV more positive than in pure 0.1 M sulfuric acid. At the same time the critical potential was shifted about 100 mV more anodic in the respective current–potential curves.

## ■ ASSOCIATED CONTENT

**Supporting Information.** Experimental details, high-resolution Auger data (Figure S1), STM (Figure S2), in situ XRD and detailed reciprocal space (Figures 3 and S4), SEM on the thiol-modified surfaces after polarization (Figure S5), and EAM (Figure S6). This material is available free of charge via the Internet at <http://pubs.acs.org>.

## ■ AUTHOR INFORMATION

**Corresponding Author**  
[renner@mpie.de](mailto:renner@mpie.de)

### Author Contributions

<sup>5</sup>G.N.A., S.B., and A.B. contributed equally to the work in this manuscript.

## ■ ACKNOWLEDGMENT

G.N.A. acknowledges a scholarship by IMPRS-SURMAT. Synchrotron radiation beamtime was provided by ESRF and we acknowledge the technical support of L. Andre, H. Isern, J. Roy, and J. Zegenhagen at beamline ID32.

## ■ REFERENCES

- (1) Schmitt, G. Global Needs for Knowledge Dissemination, Research, and Development in Materials Deterioration and Corrosion Control, White Paper, *World Corrosion Organization*, May 2009, available at [www.corrosion.org](http://www.corrosion.org).
- (2) Newman, R. C. *Stress Corrosion Cracking Mechanisms: Corrosion Mechanisms in Theory and Practice*, 2nd ed.; Marcel Dekker: New York, 2002.
- (3) Pickering, H. W.; Swann, P. R. *Corrosion* **1963**, *19*, 373–389.
- (4) Liu, M.; Schmutz, P.; Zanna, S.; Seyeux, A.; Ardelean, H.; Song, G.; Atrens, A.; Marcus, P. *Corros. Sci.* **2010**, *52*, 562–578.
- (5) Hunt, L. B. *Gold. Bull.* **1976**, *9*, 24.
- (6) Lechtman, H. *Sci. Am.* **1984**, *250*, 38 ( ).
- (7) Raney, M. Method of producing Finely Divided Nickel. U.S. Patent 1628190, 1927.
- (8) Mani, P.; Srivastava, R.; Strasser, P. *J. Phys. Chem. C* **2008**, *112*, 2770–2778.
- (9) Strasser, P.; Koh, S.; Anniyev, T.; Greeley, J.; More, K.; Yu, C.; Liu, Z.; Kaya, S.; Nordlund, D.; Ogasawara, H.; Toney, M. F.; Nilsson, A. *Nature Chem.* **2010**, *2*, 454–460. Oezaslan, M.; Strasser, P. *J. Power Sources* **2011**, *196*, 5240.
- (10) Gasteiger, H. A.; Markovic, N. M. *Science* **2009**, *324*, 48.
- (11) Hieda, M.; Garcia, R.; Dixon, M.; Daniel, T.; Allara, D.; Chana, M. H. W. *Appl. Phys. Lett.* **2004**, *84*, 628–630.
- (12) Weissmuller, J.; Newman, R. C.; Jin, H. J.; Hodge, A. M.; Kysar, J. W. *MRS Bull.* **2009**, *34*, 577–586.
- (13) Biener, J.; Hodge, A. M.; Hamza, A. V.; Hsiung, L. M.; Satcher, J. H., Jr. *J. App. Phys.* **2005**, *97*, 024301–4.
- (14) Ding, Y.; Chen, M. W.; Erlebacher, J. *J. Am. Chem. Soc.* **2004**, *126*, 6876–6877.
- (15) Weissmuller, J.; Viswanath, R. N.; Kramer, D.; Zimmer, P.; Würschum, R.; Gleiter, H. *Science* **2003**, *300*, 312–315.
- (16) Erlebacher, J.; Seshadri, R. *MRS Bull.* **2009**, *34*, 561–566.
- (17) (a) Wittstock, A.; Biener, J.; Bäumer, M. *Phys. Chem. Chem. Phys.* **2010**, *12*, 12919–12930. (b) Moskaleva, L. V.; Roehe, S.; Wittstock, A.; Zielasek, V.; Klüner, T.; Neyman, K. M.; Bäumer, M. *Phys. Chem. Chem. Phys.* **2011**, *13*, 4529.
- (18) Wittstock, A.; Zielasek, V.; Biener, J.; Friend, C. M.; Baeumer, M. *Science* **2010**, *327*, 319–322.
- (19) Ding, Y.; Chen, M. *MRS Bull.* **2009**, *34*, 569–576.
- (20) Forty, A. J.; Durkin, P. *Philos. Mag.* **1980**, *A 42*, 295–318.
- (21) Pickering, H. W.; Wagner, C. *J. Electrochem. Soc.* **1967**, *114*, 698–706.
- (22) Sieradzki, K.; Newmann, R. C. *J. Electrochem. Soc.* **1986**, *133*, 1979–1980.
- (23) Sieradzki, K.; Corderman, R. R.; Shukla, K.; Newman, R. C. *Philos. Mag.* **1989**, *59*, 713–746.
- (24) Eckstein, G. A. Dissertation, Erlangen, 2001.
- (25) Rugolo, J.; Erlebacher, J.; Sieradzki, K. *Nat. Mater.* **2006**, *5*, 946–949.
- (26) Erlebacher, J.; Aziz, M. J.; Karma, A.; Dimitrov, N.; Sieradzki, K. *Nature* **2001**, *410*, 450–453.
- (27) Erlebacher, J. *J. Electrochem. Soc.* **2004**, *151*, C614.
- (28) Moffat, T. P.; Fan, F. R. F.; Bard, A. J. *J. Electrochem. Soc.* **1991**, *138*, 3224–3235.
- (29) Chen, J. S.; Sanz, F.; Ogletree, D. F.; Hallmark, V. M.; Devine, T. M.; Salmeron, M. *Surf. Sci.* **1993**, *292*, 289–297.
- (30) Dursun, A.; Pugh, D. V.; Corcoran, S. G. *J. Electrochem. Soc.* **2003**, *150*, B355–B360.



- (31) Ding, Y.; Kim, Y. J.; Erlebacher, J. *Adv. Mater.* **2004**, *16*, 1897–1900.
- (32) Pugh, D. V.; Dursun, A.; Corcoran, S. G. *J. Electrochem. Soc.* **2005**, *152*, B455–B459.
- (33) Parida, S.; Kramer, D.; Volkert, C. A.; Rösner, H.; Erlebacher, J.; Weissmüller, J. *Phys. Rev. Lett.* **2006**, *97* (035504), 1–4.
- (34) Kaiser, H.; Eckstein, G. A. Corrosion of alloys. In *Encyclopedia of Electrochemistry*, Vol.4; Wiley-VCH: Weinheim, Germany, 2003.
- (35) Renner, F. U. Dissertation, Stuttgart, 2004.
- (36) Stratmann, M.; Rohwerder, M. *Nature* **2001**, *410*, 420–422.
- (37) (a) Renner, F. U.; Stierle, A.; Dosch, H.; Kolb, D. M.; Lee, T. L.; Zegenhagen, J. *Nature* **2006**, *439*, 707–710. (b) Renner, F. U.; Stierle, A.; Dosch, H.; Kolb, D. M.; Lee, T. L.; Zegenhagen, J. *Phys. Rev. B* **2008**, *77*, 235433–10.
- (38) Renner, F. U.; Stierle, A.; Dosch, H.; Kolb, D. M.; Zegenhagen, J. *Electrochem. Commun.* **2007**, *9*, 1639–1642.
- (39) Renner, F. U.; Gründer, Y.; Lyman, P. F.; Zegenhagen, J. *Thin Solid Films* **2007**, *515*, 5574–5580.
- (40) Bach, C. E.; Nichols, R. J.; Beckmann, W.; Meyer, H. *J. Electrochem. Soc.* **1993**, *140*, 1281–1284.
- (41) (a) Trevor, D. J.; Chidsey, E. D.; Loiacono, D. N. *Phys. Rev. Lett.* **1988**, *62*, 929. (b) Alonso, C.; Salvarezza, R. C.; Vara, J. M.; Arvia, A. J. *Electrochim. Acta* **1990**, *35*, 1331–1336. (c) Giesen, M.; Kolb, D. M. *Surf. Sci.* **2000**, *468*, 149–164. (d) Giesen, M. *Prog. Surf. Sci.* **2001**, *68*, 1–153. (e) Wiechers, J.; Twomey, T.; Kolb, D. M.; Behm, R. J. *J. Electroanal. Chem.* **1988**, *248*, 451–460.
- (42) Li, R.; Sieradzki, K. *Phys. Rev. Lett.* **1991**, *68*, 1168–1171.
- (43) Dursun, A.; Pugh, D. V.; Corcoran, S. G. *Electrochem. Solid-State Lett.* **2003**, *6*, B32.
- (44) Wagner, K.; Brankovic, S. R.; Dimitrov, N.; Sieradzki, K. *J. Electrochem. Soc.* **1997**, *144*, 3545–3555.
- (45) Vericat, C.; Vela, M. E.; Benitez, G.; Carro, P.; Salvarezza, R. C. *Chem. Soc. Rev.* **2010**, *39*, 1805–1834.
- (46) Kibler, L. A.; El-Aziz, A. M.; Hoyer, R.; Kolb, D. M. *Angew. Chem., Int. Ed.* **2005**, *44*, 2080.
- (47) Gerischer, H. *Werkst. Korros.* **1961**, *12*, 608–613.
- (48) (a) Kumar, A.; Whitesides, G. M. *Appl. Phys. Lett.* **1993**, *63*, 2002–2004. (b) Delamarche, E.; Geissler, M.; Wolf, H.; Michel, B. *J. Am. Chem. Soc.* **2002**, *124*, 3834–3835. (c) Perl, A.; Reinhoudt, D. N.; Huskens, J. *Adv. Mater.* **2009**, *21*, 2257–2268.
- (49) (a) Mayrhofer, K. J. J.; Hartl, K.; Juhart, V.; Arentz, M. *J. Am. Chem. Soc.* **2009**, *131*, 16348. (b) Ramirez-Caballero, G. E.; Ma, Y.; Callejas-Tovar, R.; Balbuena, P. B. *Phys. Chem. Chem. Phys.* **2009**, *12*, 2209. (c) Greeley, J.; Nørskov, J. K. *J. Phys. Chem. C* **2009**, *113*, 4932.
- (50) Renner, F. U.; Eckstein, G. A.; Lymperakis, L.; Dakkouri-Baldauf, A.; Rohwerder, M.; Neugebauer, J.; Stratmann, M. *Electrochim. Acta* **2011**, *56*, 1694–1700.
- (51) (a) Smigelskas, A. D.; Kirkendall, E. O. *Trans. AIME* **1947**, *171*, 130. (b) Nakajima, H. *J. Miner. Met. Mater. Soc.* **1997**, *49*, 15.
- (52) Erlebacher, J. *Phys. Rev. Lett.* **2011**, *108*, 225504.
- (53) Torres, E.; Blumenau, A. T.; Biedermann, P. U. *Phys. Rev. B* **2009**, *79*, 075441–4. 55.
- (54) (a) Gao, W.; Keith, J. A.; Anton, J.; Jacob, T. *J. Am. Chem. Soc.* **2010**, *132*, 18377–18385. (b) Venkatachalam, S.; Kaghazchi, P.; Kibler, L. A.; Kolb, D. M.; Jacob, T. *Chem. Phys. Lett.* **2008**, *455*, 47–51. (c) Luquea, N. B.; Ibach, H.; Pötting, K.; Schmickler, W. *Electrochim. Acta* **2010**, *55*, 5411–5413. (d) Valtiner, M.; Todorova, M.; Neugebauer, J. *Phys. Rev. B* **2010**, *82*, 165418–165423. (e) Valtiner, M.; Todorova, M.; Grundmeier, G.; Neugebauer, J. *Phys. Rev. Lett.* **2009**, *103*, 065502 1–065502 4.